# Application of an extended Kalman filter approach to inversion of time-lapse electrical resistivity imaging data for monitoring recharge

Vanessa Nenna,[1] Adam Pidlisecky,[2] and Rosemary Knight[1]

[1] We apply an extended Kalman filter (EKF) approach to inversion of time-lapse electrical resistivity imaging (ERI) field data. The EKF is a method of time series signal processing that incorporates both a state evolution model, describing changes in the physical system, and an observation model, incorporating the physics of the electrical resistivity measurement. We test the feasibility of using an EKF approach to inverting ERI data collected with 2-D surface array geometries. As a first test, we invert synthetic data generated using a simulated recharge event and water saturation distributions converted to electrical conductivity values using an Archie's law relationship. In the synthetic example we demonstrate the impact that the noise structure of the state evolution and the regularization weight have on EKF-estimated model parameters and errors. We then apply the method to inversion of field data collected to monitor changes in electrical conductivity beneath a recharge pond that is part of an aquifer storage and recovery project in northern California. Using lines of electrodes buried at a depth of 0.25 m when the base of the pond is dry, we monitor the wetting front associated with the diversion of stormflow runoff to the pond. Using field data, we demonstrate that by oversampling in time, we are able to apply the so-called random walk model for the state evolution and to build the model of observation noise directly from collected data. EKF-estimated values track changes in conductivity associated with both increasing water content in subsurface sediments and changes in the properties of the pore water, showing the method is a feasible approach for inversion of time-lapse ERI field data.

## 1. Introduction

[2] The processes governing the subsurface flow behavior of water impact both natural and managed recharge of groundwater aquifers. In this study, we assess the use of a geophysical method, electrical resistivity imaging (ERI), to track directly the wetting front beneath an artificial recharge pond in northern California. Our long-term objective is to use ERI to quantify spatial and temporal variation in infiltration rates, information needed to develop an improved understanding of the rate-controlling processes. ERI has been demonstrated as a means of monitoring fluid flow in the subsurface because of the sensitivity of the electrical conductivity structure to water content in the vadose zone [*Daily et al.*, 1992; *Park*, 1998]. Electrical resistivity imaging uses the relationship between injected current and measured potentials, as described by Poisson's equation subject to appropriate boundary conditions, to determine the electrical conductivity structure of the subsurface:

$$-\nabla \cdot (\boldsymbol{\sigma} \, \nabla \boldsymbol{\phi}) = I[\delta(\mathbf{r} - \mathbf{r}_{s+}) - \delta(\mathbf{r} - \mathbf{r}_{s-})]. \tag{1}$$

In (1), $\boldsymbol{\sigma}$ is the electrical conductivity structure, $\boldsymbol{\phi}$ is the electric potential field, $I$ is the injected current, and $\mathbf{r}_{s+}$ and $\mathbf{r}_{s-}$ are the source and sink electrode positions, respectively.

[3] The electrical conductivity structure is estimated on the basis of the measured potential data and the applied current configurations. By repeatedly acquiring images of the same region at different times, we can conduct a time-lapse imaging experiment from which changes in conductivity structure with time can be identified. Using appropriate rock physics relationships between electrical conductivity and subsurface material properties, it is possible to transform the observed variations in the conductivity structure with time to changes in water content with time, allowing us to image a wetting front below a recharge pond.

[4] Our interest in this study is to acquire a data set with a high rate of temporal sampling that allows us to explore a new way of approaching the inversion of time-lapse data for monitoring subsurface flow. Specifically, we are interested

[1]Geophysics Department, Stanford University, Stanford, California, USA.
[2]Department of Geoscience, University of Calgary, Calgary, Alberta, Canada.

in assessing the use of the extended Kalman filter (EKF) in a situation where we have little prior knowledge of subsurface properties and limited information about measurement noise but extremely high sampling rates relative to the expected rate of change in the monitored physical system. We find that the EKF is well suited for application to field data acquired under such conditions.

## 1.1. Extended Kalman Filter for Time Series Processing

[5] In the same way that spatial regularization is used in the inversion of geophysical data to account for the spatial variation in the imaged system, temporal regularization can be used to account for temporal variation. An excellent approach to this problem was developed by *Kalman* [1960], who first proposed a prediction-filter method for evaluating time series data of random variables that incorporates knowledge acquired from all previous time steps into the estimation of parameters at the current time step. This process, referred to as Kalman filtering, is based on iterative updates to the expressions describing both the evolution of the measured physical system (the state evolution model) and the physics of measurements (the observation model).

[6] Of interest in our application is the extended Kalman filter, which adapts the original Kalman filter to nonlinear processes by linearizing about the current state estimation [*Anderson and Moore*, 1979]. Recently, the EKF approach has been successfully demonstrated for ERI [*Lehikoinen et al.*, 2009, 2010]. The authors consider the inversion of synthetic cross-borehole data, acquired to image changes in water content in the vadose zone (i.e., the subsurface target of interest in our study). In order to account for the changes in the physical state of the system, the aspect of the EKF approach that addresses temporal regularization, the authors use a stochastic Richards' equation to simulate changes in the water content distribution. These two studies show the improvement realized by using an EKF approach instead of a frame-by-frame inversion scheme. Specifically, they show that the relative norm of the estimation error is lower for obtained model parameters. The authors also cite previous studies demonstrating that the EKF yields error estimates for each time step based on linearization of the state and observation models, which can only be attained with a frame-by-frame estimation if the residual and regularization functionals are incorporated as statistical models [*Kaipio and Somersalo*, 2004; *Lehikoinen et al.*, 2009].

[7] In this study we build upon these previous demonstrations of improved inversion results with the EKF to demonstrate the value for inversion of time-lapse field ERI data. Because it is a field study, our application of this method differs from previous work in an important way: as is true for most field studies, we have very little prior knowledge of subsurface properties and limited information about the noise structure for our observations or state evolution. This means that it would be impossible to model the evolution of the physical state accurately with a Richards' equation. As *Lehikoinen et al.* [2009] conclude that the modeled Richards' equation can have a large impact on final estimates of the physical structure at each time step, inaccurate modeling of the physical state would bias estimates of flow parameters determined from the imaging experiment. Therefore, we elect to adopt an approach introduced

in the medical imaging literature by *Vauhkonen et al.* [1998]. In this approach the so-called random walk model is used to represent the state evolution when it can be assumed that there is little change in the imaged conductivity structure between sequential images. Rather than address the challenge of using a Richards' equation, with essentially no information about the required subsurface parameters, we design our experiment so as to meet the requirement for using the random walk model: rapid data acquisition. Prior investigation suggests that for our acquisition geometry the discernible rate of change in the subsurface is, at most, on the order of 1 d. We sample on 1.5 h intervals. This rapid data acquisition approach has two advantages: (1) it allows us to assume a simple, linear form for the state update, and (2) we can develop models of the noise directly from the data by evaluating a number of time steps collected while the physical system does not change above the threshold of our resolution. Therefore, we can rely directly on observations in describing the state evolution and building up the noise covariance matrices, two of the main tasks in applying the Kalman filter.

## 1.2. Description of Field Problem

[8] Our field site is the Harkins Slough Recharge Pond (HSRP), an artificial recharge pond above an unconfined coastal aquifer in an agricultural region of northern California, United States. The pond is part of an aquifer storage and recovery project and has two primary functions. First, it is used to transfer diverted stormflow runoff to the aquifer to increase available resources for irrigation. Second, it replenishes the aquifer, which has been overdrawn for several decades, resulting in saltwater intrusion. The water agency in charge of operating the pond has a right to divert approximately $2.5 \times 10^6$ m$^3$ of surface water from the Harkins Slough to the pond from November to May each year. However, decreasing infiltration rates over the diversion period reduce the operational efficiency of the pond, reducing diversions to approximately $1 \times 10^6$ m$^3$ of water each year.

[9] It has been hypothesized that clogging from very fine particulates in the water column and/or bioactivity in the sands above the water table cause the observed decrease in infiltration rate. However, prior investigations of the sediments below the pond, using 1-D electrical resistivity probes recording to a depth of 2 m and grain size analysis of five 9 m cores, suggest there is a continuously saturated 0.5 m thick layer of fines-rich sediment at the surface, with medium to coarse-grained sand below this layer [*Pidlisecky and Knight*, 2011]. Our current hypothesis is that infiltration rates are limited by the permeability of the fines-rich layer, while initial rates are increased as a result of tilling of the pond base to a depth of ~1 m prior to the diversion season. However, to gauge which parameters and processes control infiltration rates requires a better understanding of the flow behavior directly below the pond.

## 2. Extended Kalman Filter

[10] Much of the methodology for the application of the EKF to electrical resistivity data has been developed within the medical literature for electrical impedance tomography (EIT). First proposed by *Vauhkonen et al.* [1998], the EKF has been used to address temporal smearing, which results

from rapid variations in the conductivity structure with respect to the time required to collect measurements for a single image. The theory has been expanded to incorporate spatial smoothing and known internal structures, which is often required for both EIT and ERI because they are ill-posed inverse problems [*Kaipio et al.*, 1999; *Kim et al.*, 2001, 2002; *Trigo et al.*, 2004]. More recent applications have also included approximation theory to improve estimates of errors from discretization of the state and observation models and, consequently, estimates of errors in the parameter estimation [*Huttunen and Kaipio*, 2007; *Kaipio and Somersalo*, 2007].

## 2.1. Derivation of the EKF

[11] We present a derivation of the EKF below that closely follows the derivation presented by *Kim et al.* [2002] with some modifications adopted from *Lehikoinen et al.* [2009]. We consider a system of two stochastic processes describing the evolution of the changing saturation distribution (the state evolution) and the measurement process (the observation equation). These processes are represented by (2) and (3), respectively:

$$\mathbf{m}_{k+1} = \mathbf{F}_k \mathbf{m}_k + \boldsymbol{\omega}_k. \tag{2}$$

$$\mathbf{U}_k = \mathbf{V}_k(\mathbf{m}_k) + \boldsymbol{\upsilon}_k. \tag{3}$$

Here $\mathbf{m}_k$ is a vector of log conductivity model parameters at time index $k$, $\mathbf{F}_k$ is the state evolution matrix, and $\boldsymbol{\omega}_k$ is the system noise. We adopt a log conductivity model space, conventional in inverting ERI data, as opposed to the conductivity model space used by *Kim et al.* [2002]. This imposes nonnegativity constraints and limits the dynamic range of model estimates.

[12] In (3), $\mathbf{U}_k$ represents predicted potential measurements acquired from using the nonlinear measurement process $\mathbf{V}_k$, operating on the log conductivity structure $\mathbf{m}_k$, with measurement noise $\boldsymbol{\upsilon}_k$. $\mathbf{V}$ contains information on the location of source and potential electrodes as well as the physics of current flow given by Poisson's equation (1) with appropriate boundary conditions. We consider that in both the state and observation systems the noise $\boldsymbol{\omega}$ and $\boldsymbol{\upsilon}$ have covariance matrices $\Gamma_\omega$ and $\Gamma_\upsilon$, respectively. Construction of these covariance matrices is described in sections 3.3 and 4.2.

[13] Linearization about the latest estimate of the state or model structure $\mathbf{m}_k$ transforms (3) into

$$\mathbf{U}_k = \mathbf{V}_k(\mathbf{m}_{k|k-1}) + \mathbf{J}_k(\mathbf{m}_{k|k-1})(\mathbf{m}_k - \mathbf{m}_{k|k-1}) + \mathrm{HOT} + \boldsymbol{\upsilon}_k. \tag{4}$$

In equation (4), HOT represents higher-order terms, which are assumed to be small in comparison to the first-order term. In the above notation the subscript $k|k-1$ represents an estimate of the parameter at time step $k$ based on the parameter estimate at $k-1$. This notation for predicted parameters is adopted throughout the derivation. As done by *Kim et al.* [2002], we define a pseudomeasurement to separate out terms dependent on $\mathbf{m}_k$:

$$\mathbf{y}_k \equiv \mathbf{U}_k - \mathbf{V}_k(\mathbf{m}_{k|k-1}) + \mathbf{J}_k(\mathbf{m}_{k|k-1})\mathbf{m}_{k|k-1} + \bar{\boldsymbol{\upsilon}}_k, \tag{5}$$

where $\bar{\boldsymbol{\upsilon}}_k$ is the modified error vector incorporating $\boldsymbol{\upsilon}_k$ and higher-order terms from the linearization about the current

estimate of conductivity. We update $\Gamma_\upsilon$ to $\bar{\Gamma}_\upsilon$ to include the additional errors of this estimation.

[14] The cost functional to be minimized in estimating the log conductivity model is expressed as

$$\min \frac{1}{2} \left\{ \left\| \mathbf{m}_k - \mathbf{m}_{k|k-1} \right\|^2_{\mathbf{C}^{-1}_{k|k-1}} + \left\| \mathbf{y}_k - \mathbf{J}_k(\mathbf{m}_{k|k-1})\mathbf{m}_k \right\|^2_{\bar{\Gamma}_k^{-1}} \right. \\ \left. + \alpha^2 \left\| \mathbf{R}(\mathbf{m}_k - \mathbf{m}_{\mathrm{ref}}) \right\|^2 \right\}, \tag{6}$$

where $\mathbf{R}$ is a spatial regularization matrix (e.g., a discretized Laplacian), and $\mathbf{m}_{\mathrm{ref}}$ is a reference log conductivity structure. The subscripts on the first and second terms indicate the covariance matrices used to weight the norms.

[15] Though the cost functional in (6) is different in form from the cost functionals used for several current inversion methods for ERI data (see, for example, the general formulation described by *Johnson et al.* [2010]), it does contain some similar elements. The spatial regularization, the last term in (6), has the same form commonly used for ERI data. Similarly, the first term in (6), which corresponds to the state equation (2), can be thought of as a temporal regularization term, incorporating prior information on changes to the conductivity structure with time. The second term in (6), which corresponds to the linearized observation equation (5), measures the errors between predicted and observed data.

[16] Combining the last two terms of the cost functional, as done by *Kim et al.* [2002], we can build augmented measurement vectors and matrices:

$$\bar{\mathbf{y}}_k = \begin{pmatrix} \mathbf{y}_k \\ \alpha \mathbf{R}\mathbf{m}_{\mathrm{ref}} \end{pmatrix}, \quad \mathbf{H}_k = \begin{pmatrix} \mathbf{J}_k \\ \alpha \mathbf{R} \end{pmatrix}, \quad \Gamma_k = \mathrm{block}(\bar{\Gamma}_k^\upsilon, \mathbf{I}), \tag{7}$$

which allows us to simplify the cost functional (6) to

$$\min \frac{1}{2} \left\{ \left\| \mathbf{m}_k - \mathbf{m}_{k|k-1} \right\|^2_{\mathbf{C}^{-1}_{k|k-1}} + \left\| \bar{\mathbf{y}}_k - \mathbf{H}_k\mathbf{m}_k \right\|^2_{\bar{\Gamma}_k^{-1}} \right\}. \tag{8}$$

Minimizing (8) and solving for the updates of the model error covariance matrix, we attain the prediction-filter recursions steps:

Prediction

$$\mathbf{C}_{k+1|k} = \mathbf{F}_k \mathbf{C}_k \mathbf{F}_k^T + \Gamma_k^\omega, \tag{9}$$

$$\mathbf{m}_{k+1|k} = \mathbf{F}_k \mathbf{m}_k, \tag{10}$$

Filter

$$\mathbf{G}_k = \mathbf{C}_{k|k-1} \mathbf{H}_k \left[ \mathbf{H}_k \mathbf{C}_{k|k-1} \mathbf{H}_k^T + \Gamma_k \right]^{-1}, \tag{11}$$

$$\mathbf{C}_k = [\mathbf{I} - \mathbf{G}_k \mathbf{H}_k] \mathbf{C}_{k|k-1}, \tag{12}$$

$$\mathbf{m}_{k|k} = \mathbf{m}_{k|k-1} + \mathbf{G}_k \left[ \bar{\mathbf{y}}_k - \mathbf{H}_k\mathbf{m}_{k|k-1} \right]. \tag{13}$$

[17] The prediction equations in (9) and (10) estimate the model error covariance and log conductivity structure,

respectively, on the basis of data acquired up to the $k$th time step. The predicted error covariance matrix (9) and the augmented measurement matrices (7) are used to construct the gain matrix $\mathbf{G}_k$ in (11), where $k$ in (9) and (10) has now become $k-1$. Predicted values and the gain matrix are then used to filter the estimates of the model error covariance (12) and model parameters (13) on the basis of observations collected at the new time step $k$.

[18] An important element in implementation of the EKF that does not arise in standard inversion algorithms is determination of the state evolution $\mathbf{F}_k$. As discussed above, we adopt an approach used in medical imaging to describe the state evolution: the random walk model [*Vauhkonen et al.*, 1998; *Kim et al.*, 2001, 2002]. This model approximates $\mathbf{F}_k$ as the identity matrix, making the state evolution a linear process, and requires that the estimated conductivity structure at the current time step be close to that at the previous time step. This determination of $\mathbf{F}$ is appropriate when the sampling interval is short relative to the time scale at which the imaged process evolves. In our application, we employ continuous monitoring and expect that given the short acquisition intervals (1.5 h), the physical system will look very similar between adjacent data sets (i.e., we have the advantage of oversampling in time).

### 2.2. Construction of the Noise Model

[19] Construction of the state and observation noise models is one of the primary tasks of implementing the EKF. Previous studies have used a number of approaches for determining these matrices. Early applications in medical imaging tend to use time-independent, diagonal forms for both the observation and state error covariance matrices [see, e.g., *Kaipio et al.*, 1999; *Kim et al.*, 2002; *Trigo et al.*, 2004]. More recent applications of the EKF for resistivity imaging use approximation theory, described by *Huttunen and Kaipio* [2007]. These applications focus on comparing results from numerous realizations of the physical state at each time step, based on an assumed correlation structure for the physical parameters, to results obtained using a representative homogeneous model of the state [*Lehikoinen et al.*, 2009, 2010; *Seppanen et al.*, 2009]. This introduces a new term, $\boldsymbol{\omega}^*$, into (2); the covariance of $\boldsymbol{\omega}^*$ is built on the statistics generated from the realizations. The same realizations are then used to approximate the discretization error in the observation model (3), which is included as an additional term $\boldsymbol{\upsilon}^*$. The above studies do not describe how the covariance matrices for the original terms $\boldsymbol{\omega}$ and $\boldsymbol{\upsilon}$ are generated.

[20] In this application, we invert ERI data acquired during a field experiment, where there is no prior knowledge of the subsurface correlation structure. The standard practice, when working with field data, for building the covariance matrices of observation errors is to define the covariance matrix to be a diagonal matrix with entries equal to the variances of data noise [e.g., *Day-Lewis et al.*, 2007], often with the addition of a constant level of noise [see, e.g., *Linde et al.*, 2006; *Hansen et al.*, 2008]. As the state is not explicitly modeled in most standard inversions, there is no state error covariance matrix. The model covariance used to stabilize the problem is often unknown and is, consequently, assumed to have the form of the implemented regularization [see, e.g., *Day-Lewis and Lane*,

2004]. We take a similar approach and estimate the observation error covariance directly from measurements. To find an acceptable estimate of the state covariance, we use a synthetic example to determine the sensitivity of model estimates to the variances of the state covariance matrix and the regularization weight.

## 3. Synthetic Example

[21] We simulate a recharge event in a variably saturated porous medium using COMSOL Multiphysics software. The model space for simulating recharge is 8 m across by 5 m deep and represents a simplified model of the field experiment. The model space is scaled down to increase the speed of the simulations and is divided into two horizontal layers. The hydrologic properties in each layer are assigned to be consistent with properties observed at the HSRP. The first layer is 0.1 m thick, scaled to correspond to the 0.5 m layer of fines-rich sand observed at the pond surface. The saturated permeability of this layer is defined to be $5 \times 10^{-9}$ m$^2$ with a residual saturation of 0.2 and 35% porosity. The second layer is 4.9 m thick and represents the coarse sand of the unconfined aquifer. The saturated permeability of this layer is $5 \times 10^{-8}$ m$^2$; the porosity is 40%, and the residual water content is 0.05. Although our area of focus is within the top meter of the model space, we include a thick second layer to reduce the effects of the boundary conditions on the flow simulation and conductivity inversion. Parameters governing the flow are chosen such that the saturated hydraulic conductivity is $\sim$1 m d$^{-1}$.

### 3.1. Synthetic Recharge Experiment

[22] Unsaturated flow in COMSOL is modeled using a 2-D solution to the Richards' equation in the form [*Dogan and Motz*, 2005]

$$\left[ C(h_p) + \frac{\theta}{\phi} S_s \right] \frac{\partial h_p}{\partial t} - \nabla \cdot \left[ \frac{k(h_p)\rho_w g}{\mu} \nabla (h_p + z) \right] = 0. \quad (14)$$

In the solution to (14), $h_p$, the pressure head (m), is invariant in the $y$ direction, $C$ is the specific moisture capacity, $\theta$ is the moisture content, $\phi$ is the porosity, $S_s$ is the specific storage (m$^{-1}$), $k(h_p)$ is the pressure head–dependent relative permeability, $\rho_w$ is the density of water (1000 kg m$^{-3}$), $g$ is the gravitational constant (9.8 m s$^{-2}$), and $\mu$ is the fluid viscosity (0.01 Pa s). Using a standard van Genuchten approach to estimate the water retention, or the relationship between water content and pressure head, the water content can be expressed as [*van Genuchten and Nielsen*, 1985]

$$\theta(h_p) = \theta_r + \frac{\theta_s - \theta_r}{\left[ 1 + |\alpha h_p|^n \right]^{1 - \frac{1}{n}}}, \quad (15)$$

where $\theta_s$ is the saturated liquid fraction, $\theta_r$ is the residual water content, and $\alpha$ and $n$ are empirical parameters, set here to 0.01 m$^{-1}$ and 1.5, respectively.

[23] We solve the Richards' equation for variably saturated flow from the Earth Sciences Module in COMSOL Multiphysics with a hydraulic head interpretation. We define a finite element mesh with 5816 elements and 3069 nodes.

No flow boundary conditions are set on the edges of the model space, which are sufficiently far from the area of infiltration to limit boundary effects. From 2 to 6 m along the top boundary, representing the pond base, we apply a constant head of 0.5 m, a scaled average of the pond depth during diversion. Internal boundaries between layers are set to continuity of flux. We simulate flow over 50 h and output the water saturation distribution every 1 h.

[24] Saturation values from the COMSOL simulation are exported on a regular grid of 80 × 25 cells. The exported data include regularly spaced $(x, y)$ grid locations and saturation values for each of the 51 time steps. Using an Archie's law approximation for the conductivity of the sand layers of the form [*Archie*, 1942]

$$\sigma = \sigma_w \phi^m \theta^n, \qquad (16)$$

we convert saturation to values of electrical conductivity. In (16), $\sigma_w$ is the bulk water conductivity (0.5 S m$^{-1}$), $m$ is the cementation exponent (set equal to 1.5), and $n$ is the saturation index (set equal to 2). The converted conductivity structures at a number of time steps from the simulation are included in Figure 1 for reference.
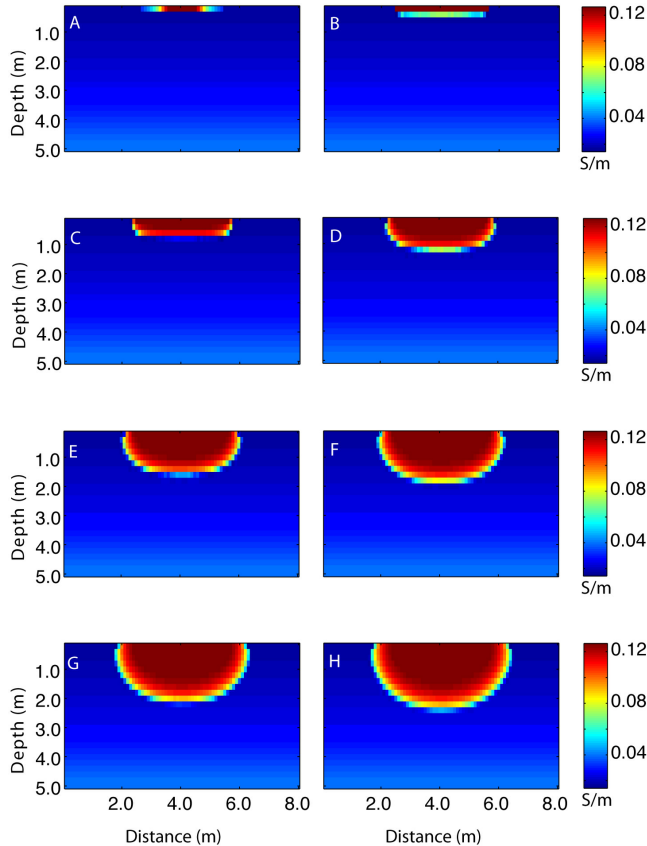


**Figure 1.** Time-lapse conductivity models created on the basis of the numerical solution to the Richards' equation for effective saturation during a recharge experiment. Conversion to conductivity is achieved through an Archie's law relationship: (a) 1 h, (b) 2 h, (c) 5 h, (d) 10 h, (e) 15 h, (f) 20 h, (g) 25 h, and (h) 30 h.

### 3.2. Observation Model

[25] Potential measurement data from the conductivity structures are simulated using the electrical resistivity forward model developed by *Pidlisecky* and *Knight* [2008]. Data are generated for 125 Wenner arrays with source-potential offsets ranging from 1 to 5 electrodes. Measurements sweep across a line of 40 equally spaced electrodes from 2 to 6 m at the top boundary of the model space. A complete data set, required to construct a single subsurface image, is acquired every hour. Taking the assumed hydraulic conductivity of 1 m d$^{-1}$ as an order of magnitude estimate of the rate of change in the system, this time interval is less than the time required for significant changes to occur in the saturation distribution within our imaged region. In other words, the sampling rate is greater than the rate of change in the physical system. This allows us to adopt the random walk model for approximating **F**. Synthetic data, generated for each conductivity structure created from the hydrologic model parameters at the 51 time steps, are contaminated with 1.5% Gaussian noise. We note that with the acquisition geometry used, the relative change in observed data between time steps after 30 h is less than 1.5%, which is the noise threshold for our measurements. We, therefore, do not expect that inversion of data after hour 30 results in meaningful updates to the estimated conductivity structure.

### 3.3. Synthetic Inversion Results

[26] We estimate the conductivity structure at each of the 51 time steps using EKF prediction-filter recursions, given in (9)–(13). In this application, we use a two-grid approach to each model update. A "fine grid" of 320 × 100 cells is used to calculate the predicted data and Jacobian, the sensitivity of measurements to changes in model parameters. Using a fine grid improves the approximation of both the data and the Jacobian, especially near source locations. A "coarse grid" of 80 × 25 cells is used to update model parameters. Estimating model parameters on a coarse grid limits the number of model parameters, making the update process more stable, and is more representative of the information content in the data.

[27] We begin by determining the discretization error associated with our forward model and, by extension, the observation equation. Using a number of conductivity structures, we forward model the predicted data on the grid used and on a finer grid, an approach similar to that described by *Lehikoinen et al.* [2010]. We determine an average error of approximately 2%, and therefore, we assume that we cannot resolve changes in the data below a 2% threshold. We use only the average error, as opposed to the full error statistics as done by *Lehikoinen et al.* [2010], to represent a situation where we have limited understanding of the noise structure, as in our field application. For the synthetic case, we set the observation error covariance to a diagonal matrix, a standard practice for field data. We use the form

$$\Gamma_v^k = \gamma \mathbf{I}\left[\text{abs}(d_k^{\text{obs}}) + \text{max}(\mathbf{d}_k^{\text{obs}})\right], \qquad (17)$$

where $\mathbf{d}_k^{\text{obs}}$ is the observed data series at time step $k$. This form is similar to the observation error used by *Lehikoinen et al.* [2010]. However, we use a single value of $\gamma$, which is

set at 2%, for both components since this is suitable for the noise of the individual datum as well as the discretization error in the synthetic data. Because we assume the rate of data acquisition to be greater than the rate of change in the imaged system, we adopt the random walk model for approximating $\mathbf{F}$, which is set to the identity matrix.

[28] To examine the sensitivity of estimated values to the variance in the state covariance matrix and regularization weight, we invert the synthetic data for a number of variances and weights. In each case we assume the covariance matrix associated with (2) has the form $\beta\mathbf{I}$, where the value of $\beta$ ranges from 1% to 30% of the mean value of the reference model. This form of the state error covariance matrix is required to be consistent with the random walk model [*Vauhkonen et al.*, 1998; *Kim et al.*, 2002], while the magnitude of $\beta$ ensures that perturbations are significant with respect to the values of the state. The regularization weight, $\alpha$, for $\beta = 0.1$ takes the values 1, 0.5, and 0.05. The initial prediction error covariance matrix $\mathbf{C}_k$ has the form $\mathbf{I}$. It has been observed that this choice for the initial form of the model error covariance matrix has little impact on the model estimates after the first few iterations because of continual updates to the covariance matrix [*Vauhkonen et al.*, 1998]. We assume a standard gradient-based smoothing operator for $\mathbf{R}$. The reference conductivity model is a homogeneous half-space with natural log conductivity $-3.6$ S m$^{-1}$.

[29] The relative norm of the estimated model errors with respect to the true conductivity structure is plotted in Figure 2 for eight combinations of $\beta$ and $\gamma$. For the first 10 h of the simulation, the error is very close for all cases. However, at later times, when there is relatively little change in the data, the estimates with larger variances and regularization weights provide better estimates. We attribute this to the decrease in the lag error, the time required for changes in the physical state to appear in estimates, with increasing variance in the state evolution [*Vauhkonen et al.*, 1998]. In Figure 3 we plot the norm of the product of the regularization matrix $\mathbf{R}$ and the model $\mathbf{m}_k$, which gives a measure of the structure in the model. Figure 3 shows that the change in the amount of structure is proportional to
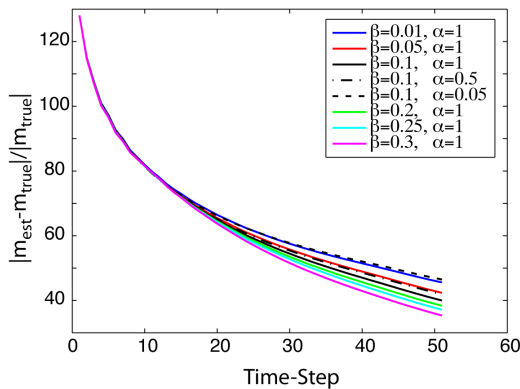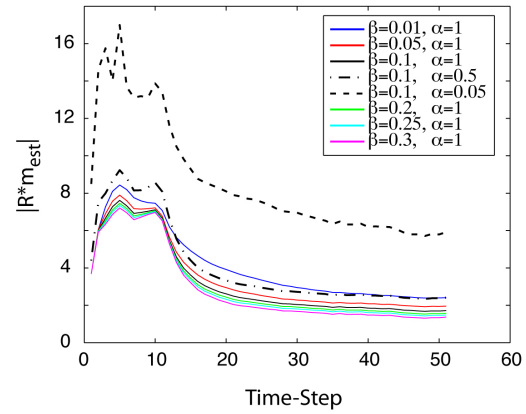


**Figure 3.** Model norm of EKF-estimated conductivity parameters from synthetic data at each time step for eight combinations of state evolution variance $\beta$ and regularization weighting $\alpha$. Larger values indicate larger amounts of structure in the estimated conductivity model.

the defined variance and inversely proportional to the regularization weighting. However, the change in structure with time is very similar for all cases. The results in Figures 2 and 3 suggest that regularization weights and variances of the state evolution have similar impacts on estimates. As these values increase, they tend to reduce the structure in model estimates, accounting for a better fit at late times when there is less structural information captured in the data.

[30] In Figure 4, we examine the impact of $\beta$ and $\gamma$ on the model error estimates, the diagonal elements of the model error covariance matrix $\mathbf{C}_k$. In Figure 4 (left) we plot the mean of the estimates, which gives information about the degree of uncertainty in the values, and in Figure 4 (right) we plot the variance of the diagonal entries, which describes their spread. As expected, larger state variances and smaller regularization weights allow for larger estimated errors of the model parameters as well as greater spreads of the estimated values. However, at each time step, the estimates normalized by the peak value for each combination of state error variance $\beta$ and regularization weight $\alpha$ yield an almost identical distribution of values. Hence, the absolute values of the model error estimates are highly dependent on the state error covariance and regularization parameter, but the structure and relative uncertainty of model estimates appear to be rather insensitive to the selection of these parameters.

[31] For reference, we plot in Figure 5 the estimated conductivity structure for the case of $\beta = 0.1$ and $\alpha = 1$ at time steps corresponding to the time steps of the "true" recharge shown in Figure 1. Overlaid on each plot are contours of the normalized model error estimates at each time step. At early times (Figures 5a–5d), the estimated conductivity structure clearly shows the lag error in both the estimated conductivities and the estimated errors. After approximately 10 iterations, however, the EKF estimates do a reasonable job capturing the change in the conductivity structure, with only a small lag in the model estimates (Figures 5e–5g). Likewise, after roughly 15 iterations the normalized error estimates tend to stabilize, and the contours showing areas of relatively high versus relatively low uncertainty within the imaged region do not change significantly.
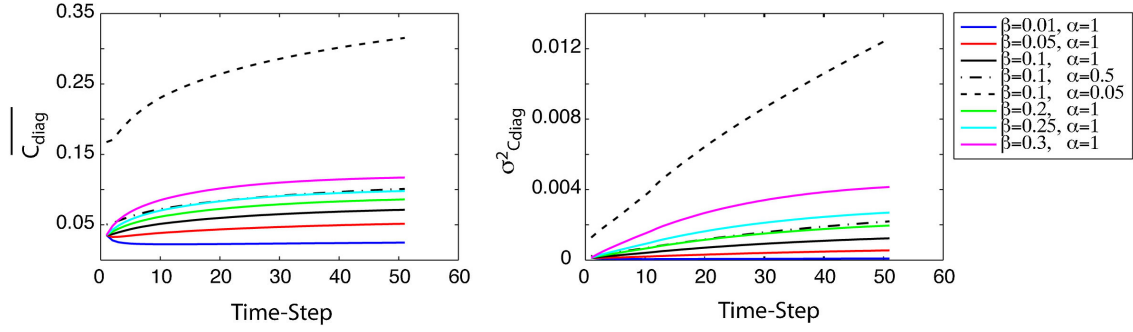


**Figure 2.** Relative model error norm of ensemble Kalman filter (EKF)–estimated conductivity parameters from synthetic data at each time step. Values are plotted for eight combinations of the state evolution variance $\beta$ and regularization weighting $\alpha$.

**Figure 4.** (left) Mean of model error estimates and (right) variance of model error estimates for EKF-estimated conductivity models at each time step for the synthetic example. Values are plotted for seven combinations of state evolution variance $\beta$ and regularization weighting $\alpha$.

## 4. Field Experiment

### 4.1. Acquisition of Field Data

[32] Prior to the diversion period in 2008–2009, we buried electrodes along two 20 m ERI lines at a depth of 0.25 m below the base of the pond, which we refer to as line 1 and line 2, and along a third 15 m line also at a depth of 0.25 m. Lines 1 and 2 consist of 40 electrodes each, with a regular separation of 0.5 m; line 3 has 30 electrodes, also

with regular 0.5 m electrode spacing. These three lines are used to image the top 5 m of the subsurface, with a focus on monitoring processes thought to control the infiltration rate. The field site is located on a map of California in Figure 6 (left), and a schematic of the field layout is included in Figure 6 (right) for reference. Surface lines are labeled L1 through L3.

[33] In addition, at either end of each of the three surface lines, we have electrical resistivity data from 1-D probes.
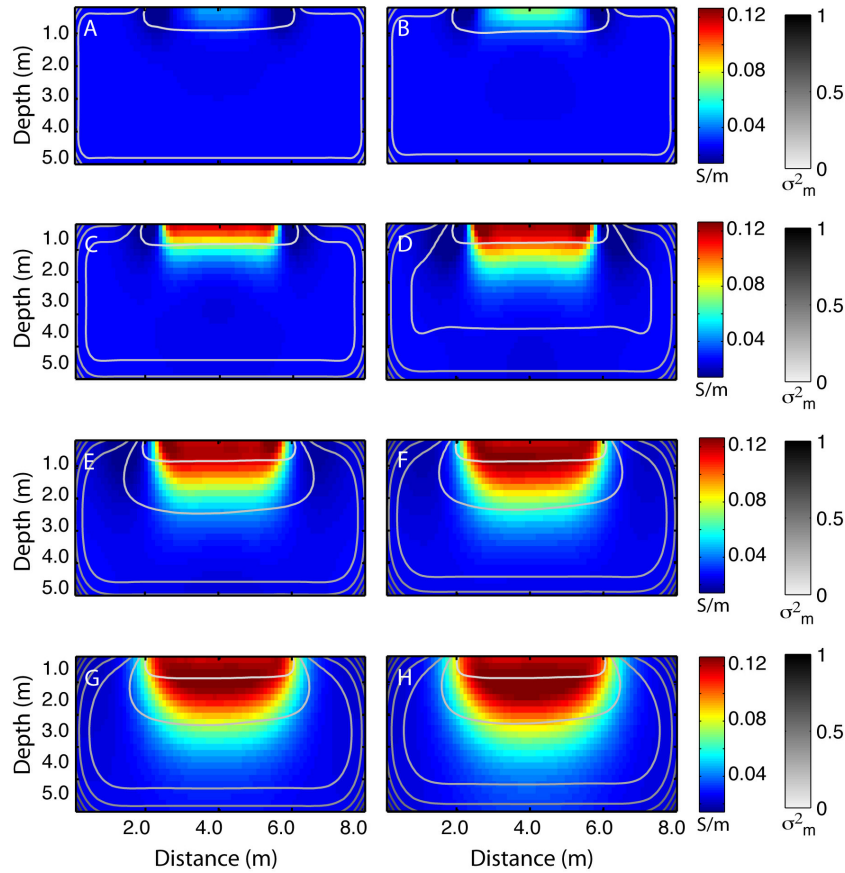


**Figure 5.** Time-lapse conductivity models estimated using the EKF from simulated data with 1.5% Gaussian noise added: (a) 1 h, (b) 2 h, (c) 5 h, (d) 10 h, (e) 15 h, (f) 20 h, (g) 25 h, and (h) 30 h. Conductivities are reported in S m$^{-1}$. Normalized estimated model errors are overlaid on the conductivity models. Low normalized variances indicate regions of less uncertainty.
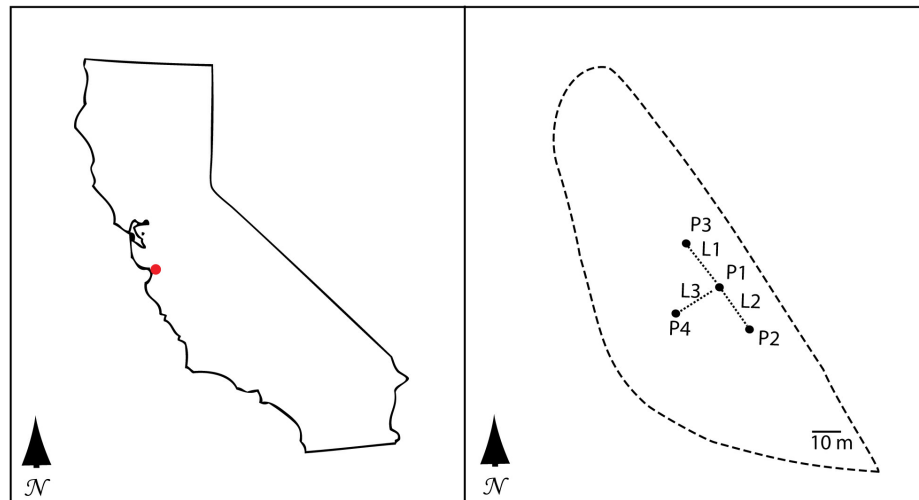
**Figure 6.** (left) Location of the Harkin Slough Recharge Pond (HSRP) on the northern California coast and (right) schematic of the field experiment for acquisition of probe and 2-D surface ERI data at the HSRP in 2008–2009. The dashed line indicates the boundaries of the pond at maximum volume.

These probes give high-resolution, 1-D measurements of the conductivity structure to 2 m depth and in the bottom 1 m of the water column. The locations of the probes, at the ends of the surface lines, provide constraints on surface data without disturbing the subsurface materials within the imaged regions. They are labeled P1 through P4 in Figure 6. The probes, described by *Pidlisecky* and *Knight* [2011] provide a first-order approximation of the time-lapse evolution of the electrical conductivity. They further provide us a measure of the bulk fluid conductivity, which is combined with water depth measurements to constrain the inversion of the surface electrical resistivity data.

[34] The acquisition of a single image of the subsurface conductivity structure for lines 1 and 2 uses 154 Wenner arrays with source potential electrode pair offsets ranging from 0.5 to 2.5 m. Line 3 uses 108 Wenner arrays with source potential electrode offsets again ranging from 0.5 to 2.5 m. Measurements are collected across the lengths of the lines in all cases. In addition, dipole-dipole arrays and non-standard four-electrode arrays are also used to collect measurements on all three lines. However, because the dipole-dipole data are of poor quality and we wish to use well-characterized arrays to test the application of the EKF to field data, we only invert measurements from the Wenner arrays here. For the three lines, collected images are available at 1.5 h intervals for 3 months during the diversion period. For each 1.5 h interval, we have one set of data acquired from each of the surface lines as well as five sets of data for each probe. Data sets collected on the probes record the 1-D structure at the beginning and end of each time interval and in between collection of data sets along the four surface lines. A number of power surges, which caused incomplete or lost data, reduced our time-lapse imaging experiment to 1936 complete data sets over approximately 18 weeks for each of the four lines.

[35] To demonstrate the use of the EKF method on field data, we focus solely on data collected along L2 in sections 4.2 and 4.3. The time-lapse inverted conductivity structure along P2, shown in Figure 7, is used to validate inversion results. Conductivity estimates along P2 are reported as relative conductivities with respect to estimates at the initial time step. Six time steps are indicated on Figure 7, which correspond to plotted two-dimensional sections. A rain event at 13.6 days, marked at A, causes observable changes in water saturation in images from all lines and probes but does not result in accumulation of significant amounts of water in the base of the pond. After the rain event, the sediments drain, and water saturation decreases (as at the time step marked B). Water diversion begins approximately 48 days after the start of the monitoring experiment,
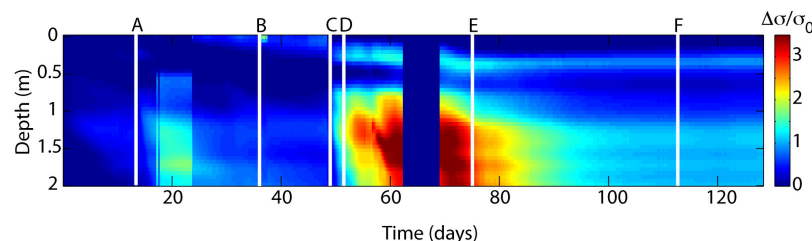


**Figure 7.** Time-lapse relative difference conductivity profile with respect to the initial conductivity profile at probe 2. Times corresponding to the time steps of inverted 2-D conductivity models are labeled A–F.

marked at C. Once the pumps are turned on, there is a significant, highly conductive water column present throughout the remainder of the imaging experiment, marked at D–F. Because electrodes are buried shallowly, this water column impacts the measured resistance values, and we need to account for the presence of water when calculating the predicted data [*Loke and Lane*, 2004]. P1, which is located on the opposite end of line 2, near the pond influx, is not included in validation of EKF results because it was miswired and provides no useable data for the 2008–2009 diversion season.

### 4.2. Application of EKF to Field Data

[36] We invert the time-lapse field data using the EKF. As before, the model covariance matrix has the form $\beta\mathbf{I}$, consistent with the random walk model of *Kim et al.* [2002], where $\beta$ is 15% of the maximum value of the reference model, and the matrix is again time invariant. We also use the same expression for the initial prediction error covariance matrix, $\mathbf{C}_k = \mathbf{I}$. The smoothing operator $\mathbf{R}$ used in the synthetic example is likewise applied here, and the weighting coefficient $\alpha$ is 1. On the basis of the results of the synthetic study, using these parameters reduces the lag in estimates while still giving reasonable weight to the observation model and regularization. The reference model is a layered model with natural log conductivity values ranging from $-4.6$ to $-6.0$ S m$^{-1}$. In this application higher conductivity values are near the surface, reflecting knowledge that there is a saturated layer at the surface while the water table is far below the base of the imaged region. Because the frequency of data acquisition is high when compared to the rate at which the physical system evolves, we again approximate $\mathbf{F}$ as the identity matrix. Two grids are still used for calculating the model update. The fine grid is $320 \times 120$ cells with $x$ and $z$ dimensions both equal to 0.125 m, and the coarse grid is $80 \times 30$ cells with 0.5 m $x$ and $z$ discretization.

[37] To determine the covariance matrix for the observation error from field data, we use a similar form to that applied in the synthetic case. However, instead of using the same $\gamma$ for both components of the noise model, as in (17), we use 2% of the maximum resistance to represent a background contribution from the discretization error. The variances of the observations, in contrast, are estimated from the data using a method for temporal compression described below.

[38] For our experiment we obtain a complete data sweep every 1.5 h. This data acquisition rate is significantly faster than the evolution of the process under consideration, and therefore, we can use temporal compression (1) to stack our data to improve the signal-to-noise ratio and (2) to estimate the variance of our data. To achieve this, we apply a method of binning the data based on the use of the coefficient of variation (the standard deviation of a measured value divided by the mean of that value) to estimate observation noise directly from the data. We use the full time series for each datum to calculate the mean and standard deviation of for a given span of time (window width). Using the mean and standard deviation for a given window centered about a given time, we calculate the coefficient of variation (COV) and assign the COV value to the midpoint of the given time window. The window is then advanced

one time step, and the process is repeated. Once the COV for a given window width has been calculated for the entire time series, the process is repeated for a wider window. The analysis is performed for window widths varying from 2 times the sampling interval to 120 times the sampling interval. We note these window widths can be adjusted to suit the signal under consideration. By the end of this process, we produce an image, for the time series associated with each datum, of the COV as a function of window width and time. An example of a composite COV for the field data set collected during the 2008–2009 diversion season can be seen in Figure 8.

[39] We use this image to calculate bin sizes for temporal compression as a function of time. Figure 8 clearly shows the nonstationary nature of the process under consideration. When we have rapid changes in the system, the COV for a given window width increases. Conversely, if we specify a desired coefficient of variation based on some understanding of our modeling (e.g., the discretization error threshold of 2%), we have different bin sizes at each point in time. Bins are larger when changes are slow and smaller when changes are rapid. We note that although our understanding of the errors involved in the modeling process may be limited, using the COV metric standardizes the binning process and is explicit about error assumptions that go into this process.

[40] We bin the entire data set, as opposed to the time series for an individual datum. To achieve this, we take the "worst case" bins across an entire data set (i.e., we take the smallest bins) by using the median of the worst 10% of all of the COVs to create a composite COV plot. That is to say, we sort all the COV values so that at a given time and for a given window width, we will have the highest COV. This requires a small bin to achieve a small COV value. While the choice of using 10% of the COVs is arbitrary, it limits the influence of outlier cases. Furthermore, along with the COV threshold, one can vary, and document, this
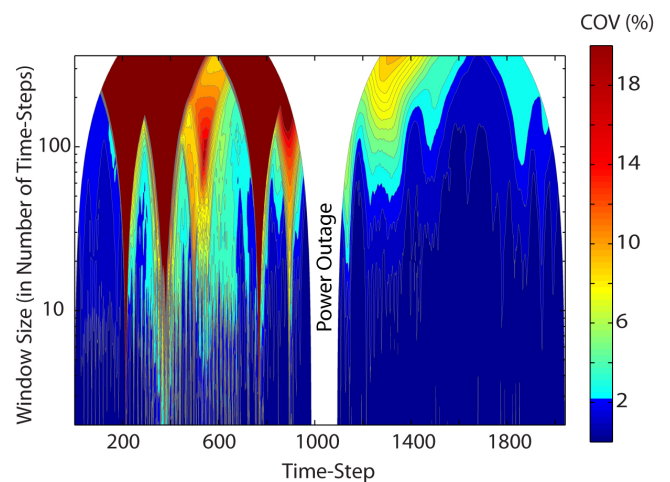


**Figure 8.** Composite coefficient of variation for data at each time step as a function of window size calculated for field data plotted on a semilog scale. A power outage resulted in lost data between time steps 988 and 1094. The 2% contour is the threshold for the bin size used to estimate measurement noise for each time window.

choice. For the data considered here, the smallest bin is 3 h, while the largest bin is 7.5 d. We note that variances estimated for windows with only a small number of time steps are less reliable than when there are a larger number of time steps per window. However, the magnitudes of the variances are fairly consistent for all time windows in this study. In the following discussion we refer to sequential time windows as opposed to time steps to denote the averaging of data.

[41] Acquiring reasonable predicted data requires that we account for the presence of the water column above the electrodes. To calculate the predicted data at each time window, we begin by using records of the water level in the pond, recorded every 15 min during the diversion period, to calculate the average water depth during the time window. At each time window we create a high-conductivity layer, where the thickness of the layer is the average water depth, and the conductivity is the bulk fluid conductivity measured on P2 during the time window. This layer is added to the subsurface conductivity structure from the previous time window, and electrode positions are set at 0.25 m below the surface regardless of the height of the water column. We calculate predicted data with the time-specific conductivity structure and acquisition geometry. Cells representing the water in the model are then made inactive, so the update is only to the estimated conductivity structure of the subsurface.

### 4.3. Results and Discussion

[42] Below we include the results from surface line 2. Similar results are observed from the other surface lines. The absolute estimated conductivity model from the data window centered at 13.6 days, approximately 12 h after the start of a rainfall event, is included as Figure 9. Figure 9 shows a high-conductivity layer near the surface, but instead of a single, uniform front, there appears to be two fronts split by a lower-conductivity zone near $-5$ m along the $x$ direction. Conductivity values tend to be slightly higher from 0 to 10 m along the $x$ axis, which is toward the center, deepest part of the pond. In Figure 10 we plot EKF-estimated conductivities for six time windows during the monitoring experiment. These estimates are all presented as the relative change in conductivity with respect to the estimated conductivity model calculated at the first time window, $k = 1$, where $k = 0$ refers to a priori values. The
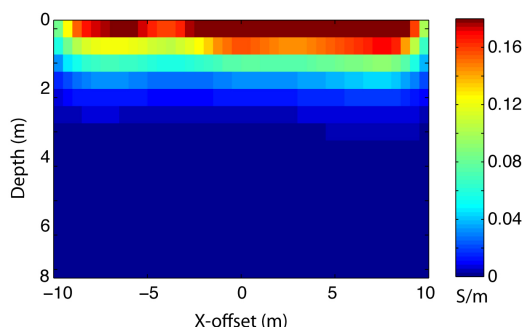
presented times coincide with times A–F marked on Figure 7. Again, the normalized variance is overlaid on the estimated parameters.

[43] The inverted conductivity models using the EKF approach capture much of the same information seen in results from probe 2, located at $-10$ m along the $x$ axis in each plot in Figure 10, suggesting the method is reliable when applied to field data. In Figures 10a–10f, there is very little change in the top layer of the conductivity model relative to the initial model, consistent with the probe data, which show that this layer remains largely saturated at all times. In Figure 10a, we plot the relative change in conductivity for the same time window shown in Figure 9. Water in the subsurface from the rain event creates a region of higher conductivity near 7 m offset in the $x$ direction, which is toward the deepest part of the pond where rainwater is most likely to pool. As in the absolute conductivity estimates, there appears to be two zones of increasing conductivity, rather than a single front. The increase in conductivity between $-5$ m and $-10$ m along the $x$ direction is consistent with observations at P2. In Figure 10b, we plot the relative change in the estimated conductivity structure at 36 days, when the saturation of the sediments has decreased. The results in Figure 10b show a decrease in saturation similar to that seen in the probe results; the high-conductivity region associated with the wetting front quickly disappears. In Figure 10c the relative conductivity structure at 48.5 days, hours after diversion to the pond begins, shows the onset of recharge with only a small increase in the conductivity in the very near surface. In Figure 10d the structure of the change in conductivity is similar to that seen in Figure 10a but is of greater magnitude. The magnitudes are also greater than those observed at the probe. We attribute this to the lag error, which reduces the absolute values of the estimated conductivity structure at the first time step, given the reference model used [*Vauhkonen et al.*, 1998]. This makes the relative changes appear greater. To account for this error, we focus on the structure of the relative change, rather than the magnitudes. We note that by choosing a very large value for the covariance at the initial time step, we can bring the initial estimate of conductivities closer to a standard frame-by-frame estimate, slightly reducing this discrepancy. However, such an approach does not fully remove the impact of the lag error on the magnitudes of the relative change in conductivity. In Figure 10e the conductivity decreases, as seen in P2, which corresponds to both a decrease in the conductivity of the pond water, shown in Figure 11, and lower infiltration rates. Figure 10f shows that the relative change in the conductivity structure again begins to increase, but the structure of the high-conductivity zone remains the same. The same increase in conductivity with time occurs in estimated conductivities at P2, though to a much smaller degree.

[44] Examining the bulk fluid conductivity as a function of time, shown in Figure 11, clearly indicates the increase in the subsurface conductivity observed at late times is a result of the increased conductivity of the pond water. This increase in conductivity after approximately 75 days of monitoring (labeled E in Figure 11) shows good correlation with the increasing temperature measured at the pond. Although temperature measurements stopped at ~95 days, the relative change in the conductivity estimates during the
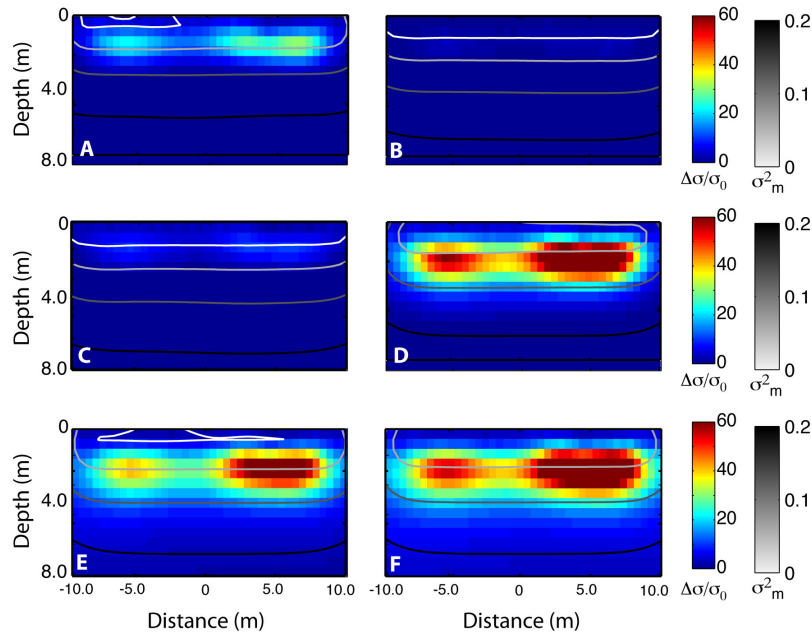


**Figure 9.** Estimated conductivity structure below L2 at 13.6 days, approximately 12 h after the start of a rainfall event. Conductivity values are reported in S m$^{-1}$.

**Figure 10.** Six time-lapse relative difference conductivity structures with respect to the initial conductivity model inverted using an EKF algorithm. Normalized estimated model errors are overlaid on the conductivity models: (a) 13.6 days, (b) 36.0 days, (c) 48.5 days (diversion begins), (d) 50.7 days, (e) 75.2 days, and (f) 112.0 days.

interval from 75 to 95 days shows good correlation between the temperature, the conductivity of the pond water, and the change in the estimated conductivities. We expect that the observed trends continued after 95 days, as temperatures increased during the summer months. From this we suggest that sediments below the first half meter of the subsurface do not fully saturate, as the absolute values of conductivity in deeper sediments are always less than in the top half meter, but that water from the pond is continuously supplied to the sediments. This is supported by the correlation between increases is the subsurface conductivity and increases in the conductivity of pond water from higher surface temperatures. The lower water content of deeper sediments despite a continuous supply of water suggests that infiltration rates are highly dependent on the hydraulic properties in the first half meter of the subsurface.

[45] The flow behavior captured by the time-lapse imaging also shows an inhomogeneous distribution of changes in saturation, with a region of lower saturation centered near $-1$ m offset in $x$. If flow were homogeneous, we would expect the conductivity to increase as a solid front. However, the absolute conductivity model at 13.6 days, shown in Figure 9, shows variability in the conductivity structure across the line. Moreover, the relative change in conductivity in Figure 10a shows significant differences in the change in conductivity throughout the imaged region, suggesting spatial variability in the amount of water that flows through the subsurface. These inversion results
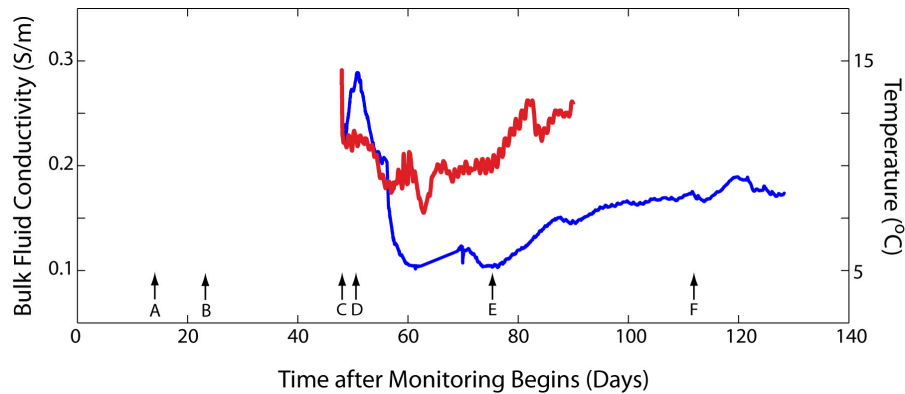


**Figure 11.** Bulk fluid conductivity (in S m$^{-1}$) as a function of time after monitoring begins (blue line) and ambient temperature at the pond (in °C; red line). Times corresponding to the time steps of inverted 2-D conductivity are labeled A–F.

indicate a complex recharge process that is not fully explained by the simple conceptual models put forward.

[46] The evolution of the normalized model error estimates also appears to respond to the changing physical conditions. Model error estimates, shown on Figure 10, are again normalized by the peak value over the entire model space. We note that the normalized values shown are very low as they cover only a small subspace of the full imaged region. Furthermore, the subspace shown is very near the sources and so should have lower uncertainties than elsewhere in the model region. As expected, in the top meter, very near the electrodes and where there is very little change in the conductivity structure, the estimated errors tend to be low. The errors then increase with depth (as in Figures 10b and 10c). However, when there is more change in the system, as in Figures 10d and 10e, there is an increase in the estimated errors within the plotted region relative to the peak value, which then stabilizes somewhat as the rate of change in the system decreases (Figure 10f). This suggests that the estimated model errors reflect uncertainties that are influenced by both spatial and temporal variations in the system.

## 5. Summary and Conclusions

[47] Previous studies have demonstrated the merits of an EKF approach to inversion of time-lapse ERI data for synthetic studies [*Lehikoinen et al.*, 2009, 2010]. Because the EKF concurrently models evolution of the monitored physical system or state and the observation process, it is an excellent approach to temporal regularization. One caveat when using an EKF approach, however, is that the update can become unstable as the number of model elements increases. Studies within the medical literature have increased model resolution by creating regions of conductivity to decrease the number of elements updated [*Trigo et al.*, 2004]. However, this requires assumptions about the shapes and locations of structures within the imaged region, which are often unknown in earth imaging. Furthermore, the filter lag causes a delay between the estimated model and model error variances and the true state at each time step. When plotting the relative change in conductivity with respect to the initial image, this can increase the magnitude of the relative changes. Although methods have been developed to reduce the filter lag [see, e.g., *Kaipio et al.*, 1999], these can only be applied after the entire time series has been processed and so could not be used in a real-time application of the EKF to monitoring experiments.

[48] In this study we demonstrate the merits of an EKF approach for field studies and highlight modifications necessary when considering field rather than synthetic studies. One of the greatest challenges in applying an EKF with field data is that we often have little information with which to develop a model of the changing physical system during imaging and even less knowledge of the associated noise structures. Determining acceptable forms for the state evolution and noise structures is one of the primary tasks in application of the EKF. Using a synthetic example, we show the sensitivity of EKF-estimated model parameters and errors to the state evolution error covariance and regularization weight. We then consider an application of the EKF to surface ERI monitoring data collected at an artificial recharge pond in northern California. Our approach to meeting the challenges of creating an acceptable model of the physical system and noise structures was to oversample our data in time. Rapid sampling of ERI data, now possible with commercially available technology, allows us to adopt the EKF for the inversion of time-lapse ERI field data.

## References

Anderson, B. D. O., and J. B. Moore (1979), *Optimal Filtering*, Prentice-Hall, Upper Saddle River, N. J.

Archie, G. E. (1942), The electrical resistivity log as an aid in determining some reservoir characteristics, *Trans. Am. Inst. Min. Metall. Pet. Eng.*, *146*, 54–62.

Daily, W., A. Ramirez, D. LaBrecque, and J. Nitao (1992), Electrical resistivity tomography of vadose water movement, *Water Resour. Res.*, *28*(5), 1429–1442, doi:10.1029/91WR03087.

Day-Lewis, F. D., and J. W. Lane Jr. (2004), Assessing the resolution-dependent utility of tomograms for geostatistics, *Geophys. Res. Lett.*, *31*, L07503, doi:10.1029/2004GL019617.

Day-Lewis, F. D., Y. Chen, and K. Singha (2007), Moment inference from tomograms, *Geophys. Res. Lett.*, *34*, L22404, doi:10.1029/2007GL031621.

Dogan, A., and L. H. Motz (2005), Saturated-unsaturated 3D (SU3D) groundwater model. I: Development, *J. Hydrol. Eng.*, *10*(6), 492–504.

Hansen, T. M., M. C. Looms, and L. Nielsen (2008), Inferring the subsurface structural covariance model using cross-borehole ground penetrating radar tomography, *Vadose Zone J.*, *7*(1), 249–262.

Huttunen, J. M. J., and J. P. Kaipio (2007), Approximation error analysis in nonlinear state estimation with an application to state-space identification, *Inverse Probl.*, *23*, 2141–2157.

Johnson, T. C., R. J. Versteeg, A. Ward, F. D. Day-Lewis, and A. Revil (2010), Improved hydrogeophysical characterization and monitoring through parallel modeling and inversion of time-domain resistivity and induced-polarization data, *Geophysics*, *75*(4), WA27–WA41, doi:10.1190/1.3475513.

Kaipio, J., and E. Somersalo (2004), *Statistical and Computational Inverse Problems, Appl. Math. Ser.*, vol. 160, Springer, Berlin.

Kaipio, J., and E. Somersalo (2007), Statistical inverse problems: Discretization, model reduction and inverse crimes, *J. Comput. Appl. Math.*, *198*, 493–504.

Kaipio, J. P., P. A. Karjalainen, E. Somersalo, and M. Vauhkonen (1999), State estimation in time-varying electrical impedance tomography, *Ann. N. Y. Acad. Sci.*, *873*(1), 430–439.

Kalman, R. E. (1960), A new approach to linear filtering and prediction problems, *J. Basic Eng.*, *82D*, 35–45.

Kim, K. Y., B. S. Kim, M. C. Kim, Y. J. Lee, and M. Vauhkonen (2001), Image reconstruction in time-varying electrical impedance tomography based on the extended Kalman filter, *Meas. Sci. Technol.*, *12*, 1032–1039.

Kim, K. Y., S. I. Kang, M. C. Kim, S. Kim, Y. J. Lee, and M. Vauhkonen (2002), Dynamic image reconstruction in electrical impedance tomography with known internal structures, *IEEE Trans. Magn.*, *38*(2), 1301–1304.

Lehikoinen, A., S. Finsterle, A. Voutilainen, M. B. Kowalsky, and J. P. Kaipio (2009), Dynamical inversion of geophysical ERT data: State estimation in the vadose zone, *Inverse Probl. Sci. Eng.*, *17*(6), 715–736.

Lehikoinen, A., J. M. J. Huttunen, S. Finsterle, M. B. Kowalsky, and J. P. Kaipio (2010), Dynamic inversion for hydrologic process monitoring with electrical resistance tomography under model uncertainties, *Water Resour. Res.*, *46*, W04513, doi:10.1029/2009WR008470.

Linde, N., A. Binley, A. Tryggvason, L. B. Pedersen, and A. Revil (2006), Improved hydrogeophysical characterization using joint inversion of cross-hole electrical resistance and ground penetrating radar traveltime data, *Water Resour. Res.*, *42*, W12404, doi:10.1029/2006WR005131.

Loke, M. H., and J. W. Lane Jr. (2004), Inversion of data from electrical resistivity imaging surveys in water-covered areas, *Explor. Geophys.*, *35*(4), 266–271.

Park, S. K. (1998), Fluid migration in the vadose zone from 3-D inversion of resistivity monitoring data, *Geophysics*, *63*(1), 41–51.

Pidlisecky, A., and R. Knight (2008), FW2_5D: A MATLAB 2.5-D electrical resistivity modeling code, *Comput. Geosci.*, *34*(12), 1645–1654.

Pidlisecky, A., and R. Knight (2011), The use of wavelet analysis to derive infiltration rates from time-lapse one-dimensional resistivity records, *Vadose Zone J.*, *10*(2), 697–705.

Seppanen, A., A. Voutilainen, and J. P. Kaipio (2009), State estimation in process tomography-reconstruction of velocity fields using EIT, *Inverse Probl.*, *25*, 085009. doi:10.1088/0266-4511/25181/085009.

Trigo, F. C., R. Gonzalez-Lima, and M. B. P. Amato (2004), Electrical impedance tomography using the extended Kalman filter, *IEEE Trans. Biomed. Eng.*, *51*(1), 72–81.

van Genuchten, M. T., and D. R. Nielsen (1985), On describing and predicting the hydraulic properties of unsaturated soils, *Ann. Geophys.*, *3*(5), 615–628.

Vauhkonen, M., P. A. Karjalainen, and J. P. Kaipio (1998), A Kalman filter approach to track fast impedance changes in electrical impedance tomography, *IEEE Trans. Biomed. Eng.*, *45*(4), 486–493.

R. Knight and V. Nenna, Geophysics Department, Stanford University, 397 Panama Mall, Stanford, CA 94305, USA. (rknight@stanford.edu; vmitchel@stanford.edu)

A. Pidlisecky, Department of Geoscience, University of Calgary, 356 Earth Sciences Bldg., 2500 University Dr. NW, Calgary, AB T2N 1N4, Canada. (adampid@ucalgary.ca)